# Improved Global Sea Surface Temperature Analyses Using Optimum Interpolation

RICHARD W. REYNOLDS AND THOMAS M. SMITH

*National Meteorological Center, NWS, NOAA, Washington, D.C.*

(Manuscript received 10 November 1992, in final form 29 August 1993)

## ABSTRACT

The new NOAA operational global sea surface temperature (SST) analysis is described. The analyses use 7 days of in situ (ship and buoy) and satellite SST. These analyses are produced weekly and daily using optimum interpolation (OI) on a 1° grid. The OI technique requires the specification of data and analysis error statistics. These statistics are derived and show that the SST rms data errors from ships are almost twice as large as the data errors from buoys or satellites. In addition, the average *e*-folding spatial error scales have been found to be 850 km in the zonal direction and 615 km in the meridional direction.

The analysis also includes a preliminary step that corrects any satellite biases relative to the in situ data using Poisson's equation. The importance of this correction is demonstrated using recent data following the 1991 eruptions of Mt. Pinatubo. The OI analysis has been computed using the in situ and bias-corrected satellite data for the period 1985 to present.

## 1. Introduction

Global sea surface temperature (SST) fields are useful for monitoring climate change, as an oceanic boundary condition for atmospheric models, and as a diagnostic tool for comparison with the SSTs produced by ocean models. Because the SSTs can be estimated from satellites, the SST field may be the best-known ocean parameter on global scales.

The blended (SST) analysis of Reynolds (1988) and Reynolds and Marsico (1993) has been widely distributed to researchers through the Tropical Oceans and Global Atmosphere (TOGA) program. The technique uses both in situ and satellite-derived SST data to produce a monthly analysis. The major advantage of this method is an objective, time-dependent correction of any satellite biases relative to the in situ data. To provide the bias correction, the technique degrades the spatial resolution of the analysis to roughly 6° lat/long.

To better preserve the high resolution of the satellite data, we have developed a new analysis technique for use operationally at the U.S. National Meteorological Center (NMC). The method uses the blended technique to provide a preliminary large-scale spatial correction of the satellite retrievals. The in situ and the corrected satellite data are then analyzed both weekly and daily using optimum interpolation (OI) on a 1° lat/long spatial grid. This method retains the bias correction while improving the spatial and temporal res-

*Corresponding author address:* Dr. Richard W. Reynolds, National Meteorological Center, NWS/NOAA, 5200 Auth Road, Room 807, Camp Springs, MD 20746.

olution of the blend. In the sections that follow, we first discuss the OI and the required error statistics. We then discuss the satellite bias correction technique.

## 2. SST data sources

The in situ SST data are obtained from the NMC file of surface marine observations. These data consist of all ship and buoy observations available to NMC on the Global Telecommunication System (GTS) within 10 h of observation time. The distribution of observations depends on shipping traffic and is most dense in the midlatitude Northern Hemisphere. There are large regions in the Southern Hemisphere with inadequate in situ sampling. This is shown in the ship and buoy distributions for the week of 4–10 August 1991 in Figs. 1 and 2. The ship data are very sparse in the midlatitude South Pacific east of the 180° meridian and in the tropical Pacific east of 160°E. The buoy data has been designed to fill in some areas with little ship data. This process of supplementing the ship data with the buoys has been most successful in the tropical Pacific. However, it should be noted that there are areas, such as the tropical Atlantic, that have almost no buoy SST observations.

The satellite observations are obtained from the Advanced Very High Resolution Radiometer (AVHRR) on the U.S. National Oceanic and Atmospheric Administration (NOAA) polar orbiting satellites. These data are produced operationally by NOAA's Environmental Satellite, Data and Information Service (NESDIS). The satellite SST retrieval algorithms are "tuned" by regression against quality controlled drifting buoy
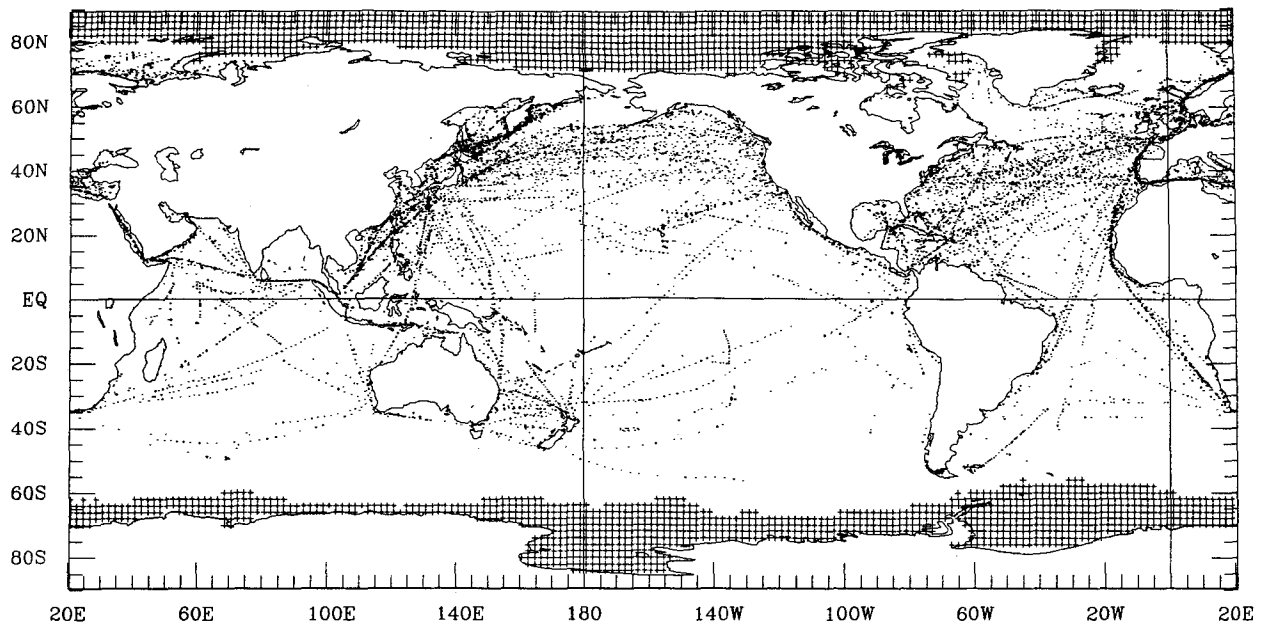
FIG. 1. Distribution of ship observations received over the GTS for the week 4–10 August 1991.
Gridded sea ice observations are indicated by a "+."

data using the multichannel SST technique of McClain et al. (1985) and Walton (1988). The tuning is done when a new satellite becomes operational or when ver-

ification with the buoy data shows increasing errors. The multichannel SST retrievals first became operational in November 1981. The algorithms are com-
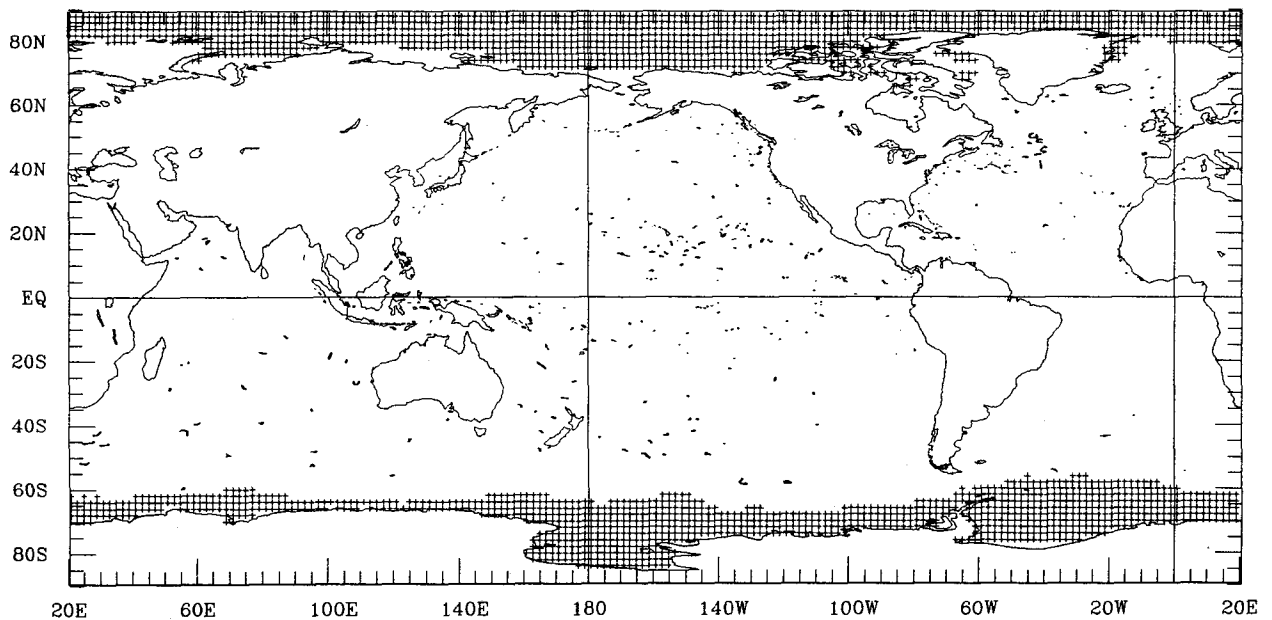
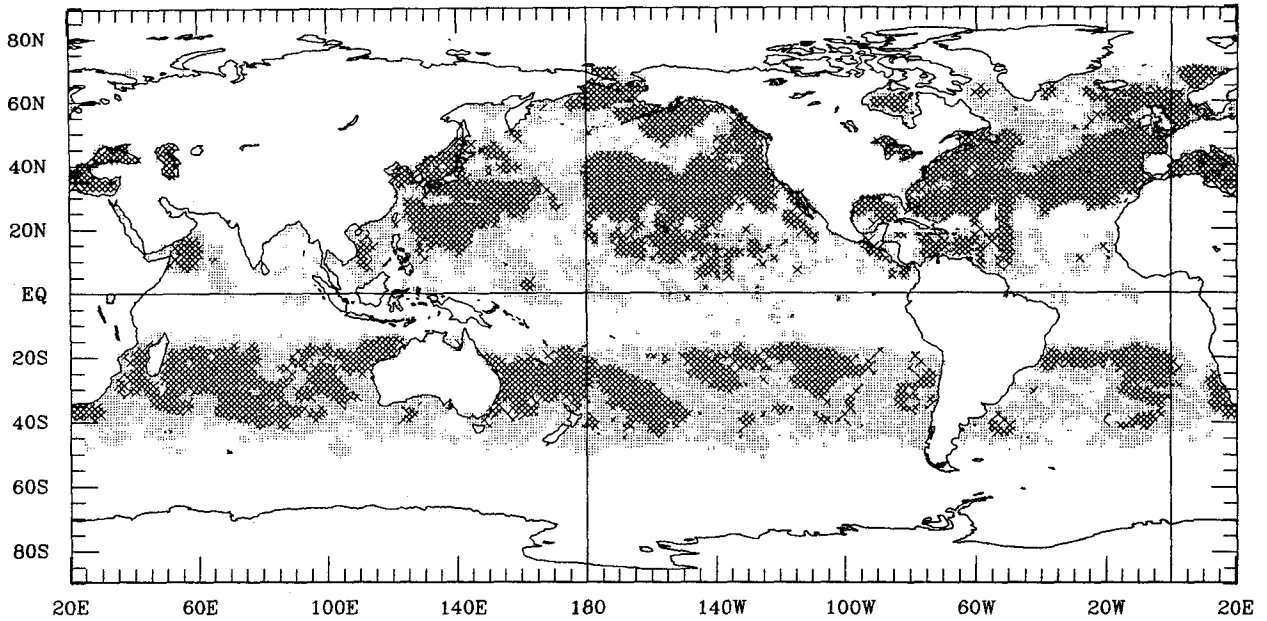FIG. 2. Distribution of buoy observations. Otherwise as in Fig. 1.

FIG. 3. Distribution of AVHRR daytime retrievals on a 1°C grid for the week 4–10 August 1991.
One to nine observations are indicated by a dot; ten or more by an "×."

puted globally and are not a function of position or time. Although the AVHRR cannot retrieve SSTs in cloud-covered regions, the spatial coverage of satellite data is much more uniform than the coverage for the in situ data. This is shown for the week of 4–10 August 1991 in Figs. 3 and 4. There, the number of weekly

daytime and nighttime observations has been averaged onto a 1° spatial grid. The sparsity of daytime observations in the tropics is unusual and was due to the effect of stratospheric aerosols from the eruptions of Mt. Pinatubo. The effect of the aerosols on the SST retrievals is discussed in more detail in section 5.
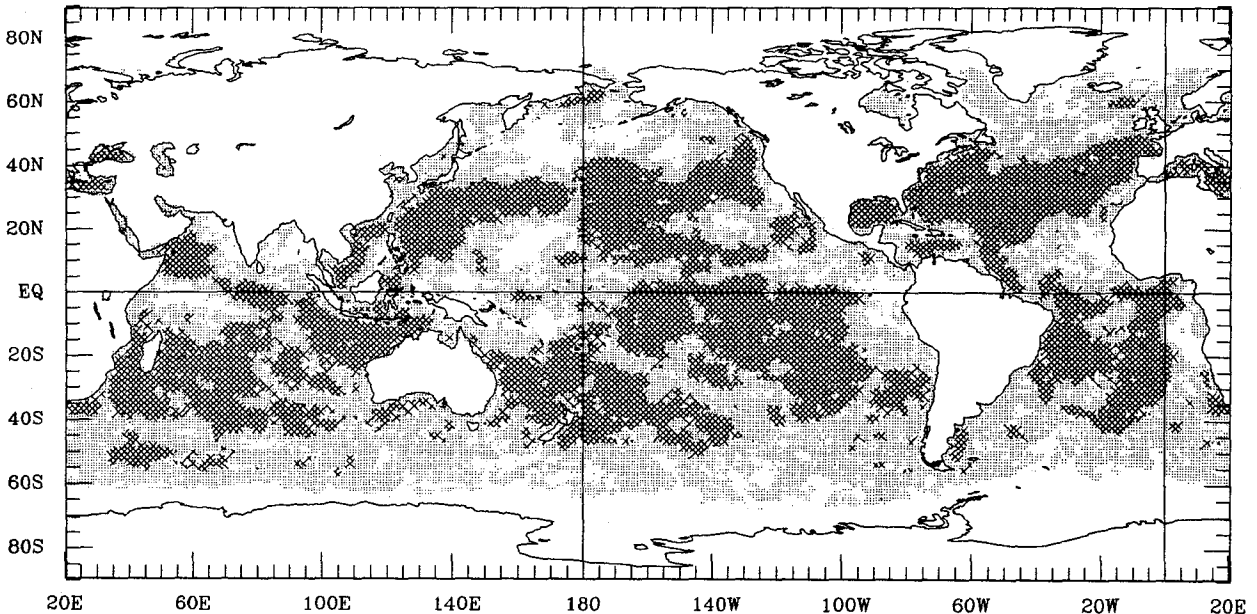


FIG. 4. Distribution of AVHRR nighttime retrievals. Otherwise as in Fig. 3.

In situ and satellite observations are sparse near the ice edge. To supplement these data, sea ice information is used. These data became available at NMC in real time in 1988 and have a 2° spatial resolution and a weekly temporal resolution. The fields combine snow coverage from NESDIS and sea ice coverage from the Navy/NOAA Joint Ice Center. If a grid box was ice covered (concentration of 50% or greater), an SST value was generated with a value of $-2$°C. The freezing point temperature of seawater with a salinity of 33 to 34 psu is $-1.8$°C. This range of salinity is typical near the ice edge in the open ocean. Thus, $-2$°C is slightly too negative. After the SST field has been computed, any SST gridded value less than $-1.8$°C is set to $-1.8$°C. The use of simulated SSTs of $-2$°C over ice-covered regions allows the analysis to reach its fixed minimum more robustly. The simulated ice observations of SST are shown in Figs. 1 and 2.

## 3. OI SST analysis

The OI SST analysis is now produced both daily and weekly on a 1° grid [e.g., see Gandin (1963) and Thiébaux and Pedder (1987) for discussion of the OI]. The weekly analysis is discussed here. The daily analysis, which is run operationally, is discussed in section 6.

Before the SST data are used in the OI they must pass the quality control procedures. These procedures include the use of programs that track ships and buoys by their identification codes and eliminate observations with unlikely position changes. All in situ observations that pass the tracking tests and all satellite retrievals are tested for accuracy of the SST. All observations are discarded if the SST value is less than $-2$°C or greater than 35°C or if the SST anomaly lies outside $\pm 3.5$ times the climatological standard deviation. These tests were designed to eliminate some of the worst data. Other procedures could be used that would be more comprehensive, however.

To reduce the number of observations used in the OI, averages over 1° squares are computed. These "super observations" are computed independently for each ship and buoy identification code and for day and night satellite retrievals. Because ships typically report only every 6 h, they usually travel through each 1° box in that time. Thus, computing 1° superobservations for each ship has little influence on the number of ship reports. The superobservations process substantially reduces the number of buoy and satellite SST reports, however. It should be noted that the day and night satellite observations are processed separately because different retrieval algorithms are used during the day and the night.

The analyses are determined relative to a first guess or predicted analysis. Following the notation of Lorenc (1981) we define two equations. The first equation gives the analysis increment at a grid point, $k$, in terms of a weighted sum of $N$ data increments. The analysis increment is defined as the difference between the analysis and the first guess; the data increment is defined as the difference between the data and the first guess. The expression for the analysis increment, $r_k$, can be written as

$$r_k = \sum_{i=1}^{N} w_{ik} q_i, \tag{1}$$

where $q_i$ are the data increments and $w_{ik}$ are the least-squares weights that are given below. The subscript $k$ ranges over the grid points where the solution is required. The subscripts $i$ and $j$ (used below) range over the data points. When (1) has been evaluated at all grid points, the analysis is completed by adding the analysis increments to the first guess at each grid point. The analysis is computed in terms of increments rather than the entire field so that the first guess is preserved in regions with little or no data. In that case the weights, $w_{ik}$, approach zero.

Our first-guess field is the analysis for the preceding week. (For the initial OI analysis, the blended analysis was used as a first guess.) Other investigators (e.g., Clancy et al. 1990) have used climatology as a first guess. There are advantages for each choice. If climatology is used, the first guess is independent of the analysis. Thus, the data increments are also independent of the analysis. Because these increments are used to define the error statistics that are required by the OI, the statistics are also independent of the analysis. In addition, the increments are, in this case, identical to SST anomalies and can be directly related to other studies. However, because time scales of SST anomalies have been found to be of the order of months (e.g., see Reynolds 1978), the analysis from the previous week is a better forecast of SST than climatology. When there is no data, the OI returns the value of the first guess. Thus, if climatology is the first guess, the OI SST anomaly would be zero. If the previous analysis is the first guess, the OI SST (in our case the SST anomaly, see discussion in section 7) simply persists. Because of this advantage, we believe that the analysis from the previous week is a better first guess than climatology.

The weights in (1) are determined by a least-squares minimization. This procedure results in a set of linear equations

$$\sum_{i=1}^{N} M_{ij} w_{ik} = \langle \pi_j \pi_k \rangle \tag{2}$$

for $j = 1, 2, \cdots, N$ and where $M_{ij}$ is defined by

$$M_{ij} = \langle \pi_i \pi_j \rangle + \epsilon_i \epsilon_j \langle \beta_i \beta_j \rangle. \tag{3}$$

Here, $\langle \pi_i \pi_j \rangle$ is the ensemble average of the first-guess correlation error and $\langle \beta_i \beta_j \rangle$ is the ensemble average of the data correlation error. The term, $\epsilon_i$, is the stan-

dard deviation of the data error normalized by the standard deviation of the guess error at point $i$. The weights, $w_{ik}$, are the optimum weights only when $\langle \pi_i \pi_j \rangle$, $\langle \beta_i \beta_j \rangle$, and $\epsilon$ are accurately known. The OI method assumes that any data biases are zero.

Because $\langle \pi_i \pi_j \rangle$, $\langle \beta_i \beta_j \rangle$, and $\epsilon$ are defined in terms of increments, they are specific to the analysis. As a starting point for the analysis, initial estimates of these terms were made. This is necessary because the statistics for $\langle \pi_i \pi_j \rangle$, $\langle \beta_i \beta_j \rangle$, and $\epsilon$ must be computed relative to the first guess that has been defined as the previous analysis. Improved estimates were derived from these initial analyses and are presented in the next section.

We initially assumed that $\langle \pi_i \pi_j \rangle$ could be represented by a negative squared exponential, or Gaussian, function given by

$$\langle \pi_i \pi_j \rangle = \exp\left[ \frac{-(x_i - x_j)^2}{\lambda^2} \right], \qquad (4)$$

where $x_i - x_j$ is the scalar distance between points $i$ and $j$ and the e-folding scale, $\lambda$, is fixed at 222 km. For in situ and ice data, we assumed that the data errors were uncorrelated, $\langle \beta_i \beta_j \rangle = \delta_{ij}$, where $\delta_{ij} = 1$ for $i = j$ and 0 for $i \neq j$. For satellite data we assumed that the data were composed of equal parts of correlated and uncorrelated error: $\langle \beta_i \beta_j \rangle = 0.5(\langle \pi_i \pi_j \rangle + \delta_{ij})$. The value of $\epsilon$ was constant for each data type unless the number of superobservations was very low (see Table 1). Because in most cases the number of ship superobservations was one while the number of satellite and buoy observations was four or more, this resulted in a value of $\epsilon = 3$ for ships and $\epsilon = 1$ for all other types of data.

The solution of the $N$ linear equations in (2) is found using Cholesky decomposition (e.g., see Stewart 1973). This procedure consists of two steps: first the matrix, $M_{ij}$, is decomposed into upper and lower triangular matrices, then the values of $w_{ij}$ are found using the decomposed matrices and the right-hand side of (2). The decomposition is computationally intensive. Because, as noted by Lorenc (1981), $M_{ij}$ does not depend on the location of the analysis points, $M_{ij}$ can be decomposed once for a number of analysis points, $k$. It would be theoretically possible to solve the OI for the entire globe by computing one decomposition of $M_{ij}$. This would not be practical due to limited computer storage and numerical instabilities due to round off, however. With some experimentation, we found that we could solve for $M_{ij}$ using all data within an 8° by 8° box. The weights in (2) were then obtained for 16 1° values that were arranged in a 4° by 4° box. The centers of the two boxes were defined to coincide. Thus, we have one matrix decomposition for each set of 16 analysis points. The 8° boxes are shifted at 4° intervals to cover our 1° global grid. The use of 8° boxes, which are larger than the 4° box defined by the grid points,

TABLE 1. Initial global assumed data to guess ratios.

| Number of superobservations | Ship | Buoy | Satellite day and night | Ice |
|---|---|---|---|---|
| 1 | 3.0 | 2.0 | 1.8 | 1.0 |
| 2 | 2.2 | 1.4 | 1.2 | 1.0 |
| 3 | 1.8 | 1.2 | 1.0 | 1.0 |
| 4 or more | 1.8 | 1.0 | 1.0 | 1.0 |

allows some overlap of the data between boxes and produces a smoother analysis. This system was designed to balance the number of observations, $N$, used in each matrix decomposition versus the number of decompositions.

If there are too many data points that are too close together, $M_{ij}$ will be nearly singular and this may lead to difficulties in obtaining a numerical solution by the above method. The averaging of the observations to form 1° superobservations was done to reduce this possibility. However, because this averaging was not done for all observations but by categories (i.e., individual ships, individual buoys, day satellite, night satellite, or ice) the decomposition of $M_{ij}$ can still be numerically unstable. If $M_{ij}$ was found to be unstable, the number of observations was reduced within a given radius, $R$, which was initially set to 25 km. If the observations were the same type (e.g., both ship observations), the observations were replaced by an averaged observation. If the observations were of different types (e.g., ship and day satellite), the observation with the lower $\epsilon$ was kept and the others were discarded. In the special case that the observations were of different types but the $\epsilon$'s were equal, the observations were averaged. If this procedure fails, then $R$ was increased by a factor of 1.5 until the solution became stable. This procedure was needed in no more than 5% of the 4° boxes for each global solution. A few of these boxes required up to four iterations of increasing $R$ before a solution was obtained.

The weekly analysis using these statistics was run from March 1990 through the end of December 1991. An example of the OI SST analysis is shown in Fig. 5 for the week 13 to 19 January 1991, a period without important satellite biases. This can be contrasted with the blended product, which is shown in Fig. 6 for a special 15-day period, 9 to 23 January 1991. The time period for the blended product was reduced to the practical minimum for that analysis scheme and chosen so that the centers of the two analysis periods coincide. The higher resolution of the OI is apparent. In the tropics, the equatorial eastern Pacific and Atlantic cold tongues are more realistically shown in the OI. At higher latitudes, the OI shows tighter gradients, particularly in the Gulf Stream, the Kuroshio and Falkland Current regions. This higher-resolution depiction qualitatively agrees with patterns shown in the satellite
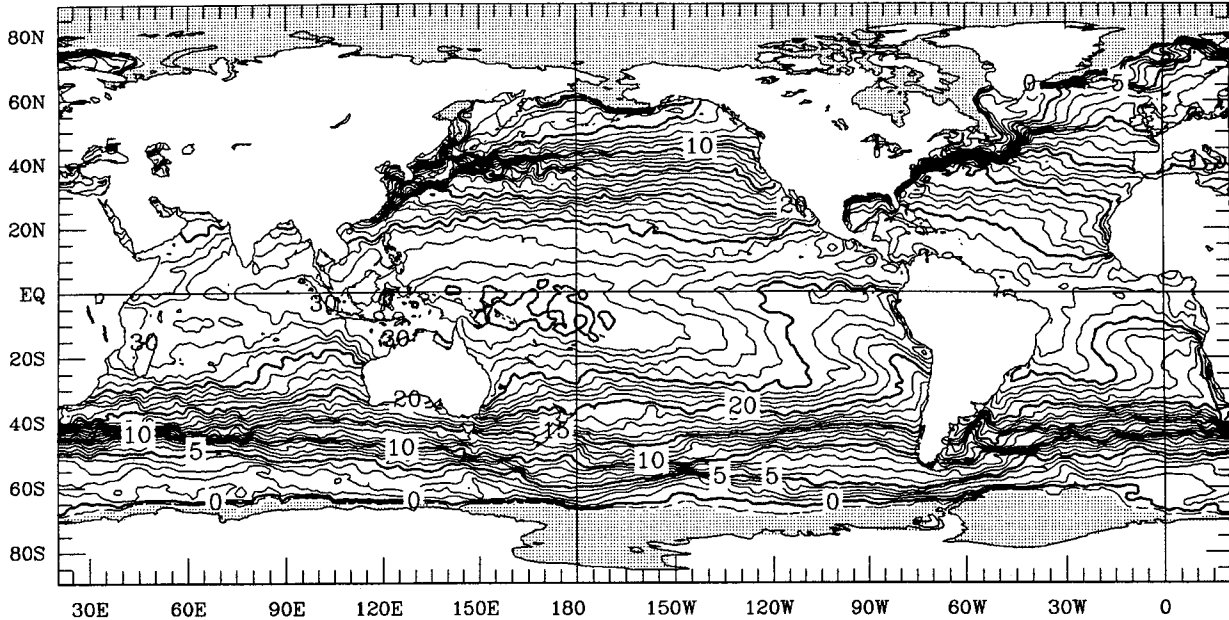
FIG. 5. Mean SST from the OI using the assumed statistics for the week 13-19 January 1991.
The contour interval is 1°C with heavy contours every 5° starting with 0. The -1°C contour is dashed; SSTs below -1.79°C are shaded.

data and the patterns simulated by high-resolution ocean models.

## 4. OI statistics

The OI is only optimal when the correlations and variances are known for the analysis increment and each type of data increment. As discussed above, the initial OI analyses of SST at NMC assumed globally constant statistics with isotropic correlations. Here, we discuss a more realistic computation of these statistics.

The data errors that will be estimated by the OI statistics originate from different sources. These include measurement errors, which are due to the expected error of making an observation, and representativeness errors, which occur because a point measurement in space and time is used to represent a spatial and temporal average. The representativeness "errors" include physical signals, such as the diurnal variations, that cannot be resolved by the OI. Some authors (e.g., Clancy et al. 1990) have estimated each type of error and then computed a total error for use in the OI. Others (e.g., Meyers et al. 1991) have used data increments to divide the error into a correlated and uncorrelated part as discussed by Thiébaux and Pedder (1987). We have chosen the second approach.

In general, the correlation between two SST observations decreases with increasing separation. Although a range of functions, $F$, can be used to determine the correlation with separation distance, we used the negative-squared exponential, or Gaussian, function given by

$$F_{xy} = A \exp\left[\frac{-(x_i - x_j)^2}{\lambda_x^2} + \frac{-(y_i - y_j)^2}{\lambda_y^2}\right]. \quad (5)$$

Here $x$ and $y$ are the coordinates in the zonal and meridional directions, respectively. The expression is similar to (4) except that (5) is no longer isotropic and allows different zonal and meridional spatial scales given by $\lambda_x$ and $\lambda_y$. This model assumes that the axes of the covariance function coincide with the zonal and meridional axes.

The variables $A$, $\lambda_x$, and $\lambda_y$ can be obtained by a (nonlinear) least-squares fit to correlations obtained using observations at all possible combinations of $(x_i - x_j)$, $(y_i - y_j)$ (M. Pedder 1993, personal communication). However, we chose to simplify this procedure by first setting $y_i = y_j$ and then $x_i = x_j$. Equation (5) reduces to two separate equations:

$$F_x = A_x \exp\left[\frac{-(x_i - x_j)^2}{\lambda_x^2}\right] \quad (6)$$

and

$$F_y = A_y \exp\left[\frac{-(y_i - y_j)^2}{\lambda_y^2}\right]. \quad (7)$$

This is the same spatial covariance model used by many others (e.g., Clancy et al. 1990; Meyers et al. 1991). The fitting procedure will determine $A_x$, $A_y$, $\lambda_x$, and $\lambda_y$ from (6) and (7). The variable $A$ in (5) is defined by the averages of $A_x$ and $A_y$, which are assumed to be ensemble estimates of $A$. As mentioned later in this
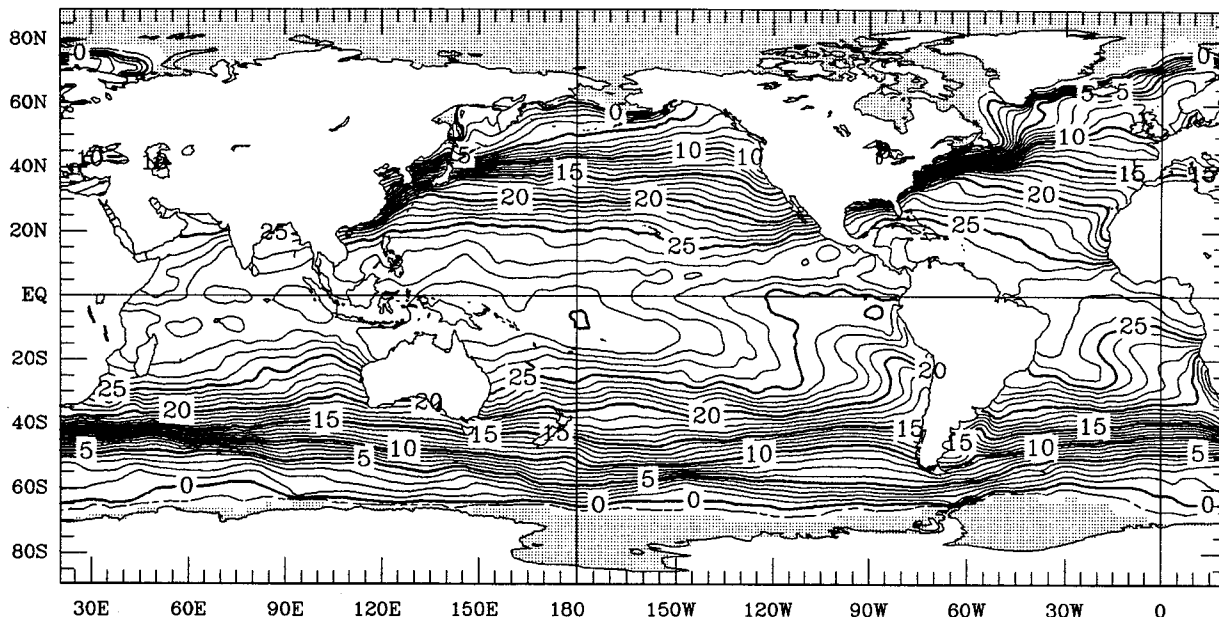
FIG. 6. Mean SST from the blended analysis for the 15-day period 9–23 January 1991. Otherwise as in Fig. 5.

section, there are many other possible assumptions for the correlation functions.

To determine $A_x$, $A_y$, $\lambda_x$, and $\lambda_y$ in (6) and (7), a 1-year period from July 1990 through June 1991 was selected. This period gives a full annual cycle, avoids any initial "spinup" problems and avoids the satellite biases that occurred after June 1991 (discussed in the following section). The statistics were determined from the 1° superobservations that had been converted to data increments. The 1° superobservations were used here because they are the observations used in the OI and the statistics must be derived from them. The superobservations include information on the average position of the observations. To simplify our computation of the statistics, this information was ignored. Thus, for each type of data, weekly increments were computed at locations centered on a 1° grid.

The data increments are assumed to consist of a correlated part, given by (6) and (7), plus an uncorrelated part. Thus, the equations will not, by themselves, have a correlation of 1.0 with a separation distance of zero. The fitting procedure uses all correlations except those at zero separation to determine $A$ and $\lambda$. Once $A$ is known, the variance can be partitioned into correlated and uncorrelated parts.

Because the OI analysis uses current data as well as a first-guess field obtained from the previous analysis, the current analysis will tend to lag behind the current data. This occurs because of a strong seasonal cycle in middle and high latitudes. During a week this change can occasionally exceed 1°. Thus, the data increments will tend to have a seasonal component. If this is not

removed, a large spatially correlated signal will remain. This signal was removed by first determining a least-squares fit to the mean and the annual and semiannual cycles and then subtracting these terms from the data increments. This was done at each grid point.

The detrended data increments were then used to compute the correlation statistics. This could have been done by computing the meridional and zonal correlations at each 1° grid point. However, even in the case of the satellite data, the results were found to be too noisy to produce stable statistics. Thus, all data within 20° latitude by longitude boxes were processed and average statistics were computed for each box. The centers of the 20° boxes were defined on a 10° global grid. Thus, the results will have an overlap of 10° in latitude and longitude. The spatial correlations and variances were computed for daytime satellite retrievals, nighttime satellite retrievals, buoy data and ship data.

In each 20° box there are a maximum of 400 (20 times 20) time series, one for each 1° grid point. The correlations were computed for all pairs in the zonal and meridional directions. To simplify the processing, correlations in each direction were separated into bins with a width of 55 km. (The bin size was selected to be less than or equal to the east–west 1° grid separation between 60°S and 60°N.) It was found that the results were not very sensitive to small changes in the bin size. For each bin the mean correlation, mean separation, and number of correlations per bin were saved for analysis. The area-average variance was also saved for each area. The fit to (6) and (7) was done using a least-
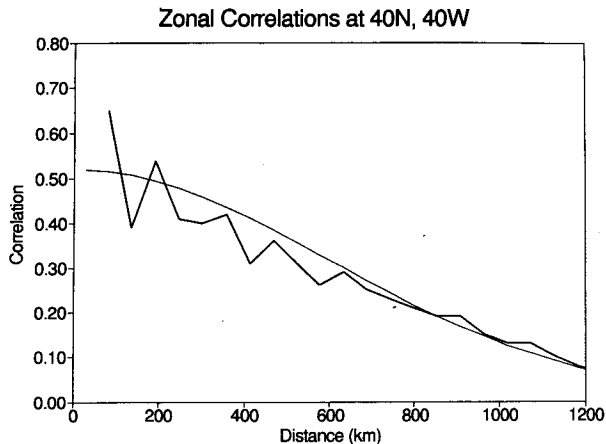
Zonal Correlations at 40N, 40W



FIG. 7. The binned correlations at 40°N and 40°W are indicated by the heavy line. The correlations were computed in the zonal direction from the daytime satellite data increments. The fitted function (6) is indicated by a light line.

Meridional Correlations at 40N, 40W



FIG. 8. The correlations at 40°N and 40°W computed in the meridional direction with fit from (7). Otherwise as in Fig. 7.

squared criteria (see the appendix for details). Because there will be more pairs with separations near 1000 km than at 100 km, all bins with data were equally weighted. This prevented correlations at middle separations from having a higher weight than correlations at small separations. Bins with separations greater than 1100 km (10° of latitude) were not used. This prevented sparse correlations at large separations from adversely effecting the fit. If less than eight bins had correlations, no fitting statistics were computed.

Examples of the binned correlations and the negative-squared-exponential fit are shown in Figs. 7 and 8. The correlations shown were computed in the zonal and meridional direction using daytime satellite data increments at 40°N, 40°W. A residual was also computed that was defined as the sum of the squares of the difference between the binned data and the fit normalized by the sum of the squares of the binned data. Both figures show fits with residuals of 2%. When all four of the satellite results (daytime zonal, nighttime zonal, daytime meridional and nighttime meridional) were combined, the average residual was 3% with a standard deviation of 3%. As shown in the figures, there is a tendency for (6) and (7) to underestimate the correlation at small and large values while overestimating the correlation at middle values. This effect would tend to overestimate the e-folding scale. As the residual increases, the overestimation becomes more evident. This may be clearly seen in Fig. 9, which shows the meridional fit at the equator and 160°W and has a residual of 5%. The zonal fit at the equator and 160°W has a residual of 4% (not shown) and also demonstrates the same tendency. (The noise in the computed correlations in Fig. 7 is due to the 55-km binning distance that tends to alternately under- and oversample some
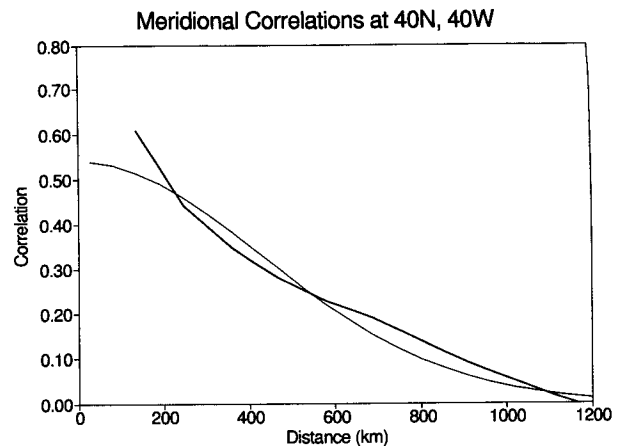
of the bins as the zonal distance between the 1° gridded data varies with latitude.)

Although, the residuals are low, a careful comparison of different fitting functions, such as that by Thiébaux et al. (1990), could find a set of functions with lower residual errors. In particular, the axes of $F_{xy}$ in (5) can be generalized so that the fitting procedure would determine the correct orientation based on the data (e.g., see Buell and Seaman 1993) rather than assuming they coincide with the coordinates. M. Pedder (1993, personal communication) suggests that the relatively constant values of the data correlations (heavy curve in Fig. 9) could be caused by a nonstationary process such as a slowly varying mean superimposed on a stationary random process. During this period, the equatorial Pacific was beginning an anomalous warming caused by the start of an El Niño–Southern Oscillation (ENSO)
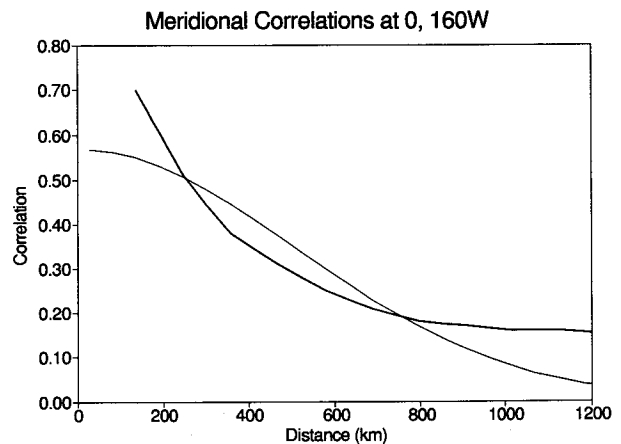
Meridional Correlations at 0, 160W



FIG. 9. The correlations at the equator and 160°W computed in the meridional direction. Otherwise as in Fig. 8.

event [ for general discussion see Rasmusson and Carpenter (1982)]. The ENSO warming is the nonstationary process suggested by Pedder. If it were removed, the *e*-folding scales would be smaller. The simplified correlation functions (6) and (7) were found to give results that were spatially noisy, however. Further computation will be deferred until more analyses have been obtained (see section 7) and a longer times series of data increments can be formed.

The computed correlations (examples were shown in Figs. 7–9) have been normalized by the total data variance, $\sigma^2$. As mentioned above, $A\sigma^2$, where the $A$ is from (5), is equal to the correlated part of the error variance while $(1 - A)\sigma^2$ is the uncorrelated part. If the data errors could be assumed uncorrelated, then the correlated error must be the guess error and $\epsilon$, the ratio of the data to guess error, would be defined by

$$\epsilon^2 = \frac{1 - A}{A} \tag{8}$$

for each data type. It should be noted that the variance of the guess should be the same for all data types.

Equations (6) and (7) were fitted to the daytime and nighttime satellite data increments for the 20° boxes centered on the global 10° grid. The difference between $A_x$ and $A_y$ was small for each data type. As mentioned earlier, $A = 0.5(A_x + A_y)$. In Fig. 10, the zonal average of $\sigma^2$ (the total, correlated plus uncorrelated, variance) and $A\sigma^2$ (the correlated variance) is shown for daytime and nighttime data. It is clear that $A\sigma^2$ is not the same for day and night. Furthermore the daytime-correlated variance is actually larger than the nighttime total variance in the Tropics.

To account for this discrepancy, we must allow the data errors to consist of a correlated and uncorrelated part. It is still assumed that the guess errors are all correlated. This guess error, which must be common for all data types, is now assumed to be the local minimum of the daytime and nighttime satellite value of $A\sigma^2$ (the correlated variance). If this value for the guess error is written as $\sigma_m^2$, then the remaining correlated error is assigned to the data and must be given by the difference, $A\sigma^2 - \sigma_m^2$. This partitioning of the correlated error between the guess and data does not affect the uncorrelated error. The uncorrelated error is still assigned to the data and has a value of $(1 - A)\sigma^2$. Of course $\sigma_m^2$ could (and probably does) include correlated data error. Thus, the guess error is less than $\sigma_m^2$. This assumption was necessary to define $\epsilon$, however. Although the assumption is arbitrary, it was the only way we could find to partition the data and guess errors in a consistent way. Because satellite measurements are made with one instrument, however, it seems reasonable to assume that satellite SSTs would have correlated errors. With these assumptions, the satellite data increments can be written as
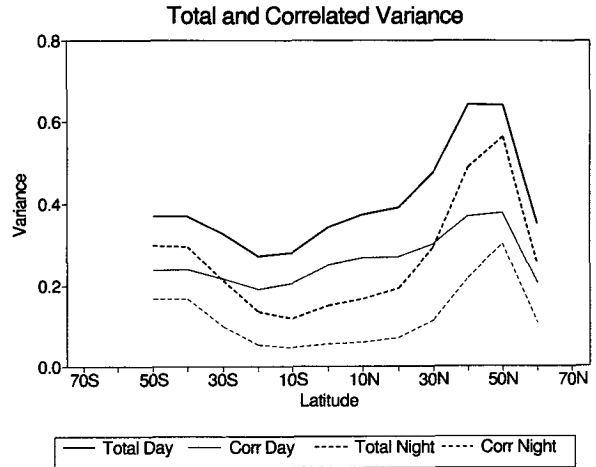


FIG. 10. Zonally averaged total (correlated plus uncorrelated) variance ($\sigma^2$) and correlated variance ($A\sigma^2$) from the daytime and nighttime satellite data.

$$\epsilon^2 = \epsilon_c^2 + \epsilon_u^2, \tag{9}$$

where $\epsilon_c$ is the correlated data to guess error and $\epsilon_u$ is the uncorrelated data to guess error given by

$$\epsilon_c^2 = \frac{A\sigma^2 - \sigma_m^2}{\sigma_m^2} \tag{10}$$

and

$$\epsilon_u^2 = \frac{(1 - A)\sigma^2}{\sigma_m^2}. \tag{11}$$

Using (10) and (11), (9) can be written as

$$\epsilon^2 = \frac{\sigma^2 - \sigma_m^2}{\sigma_m^2}.$$

The fitting procedure thus defines $\epsilon$ for the daytime and nighttime satellite data. However, they also must be defined for ships, buoys, and ice. There were not sufficient data to carry out the fitting procedure everywhere for ships and buoys. At those places where there were sufficient data, the results were spatially very noisy. Thus, just the variance, $\sigma^2$, was computed and it was assumed that the data errors were uncorrelated (i.e., $\epsilon_c = 0$). This assumption is usually made with in situ data (e.g., see Clancy et al. 1990). Because the guess error is already defined, the ratio for ships and buoys can be found by

$$\epsilon^2 = \epsilon_u^2 = \frac{\sigma^2 - \sigma_m^2}{\sigma_m^2}.$$

In the figures that follow, all fields of $\epsilon$ and $\sigma$ were smoothed by application of zonal and meridional binomial filters with weights $1/4$, $1/2$, and $1/4$.
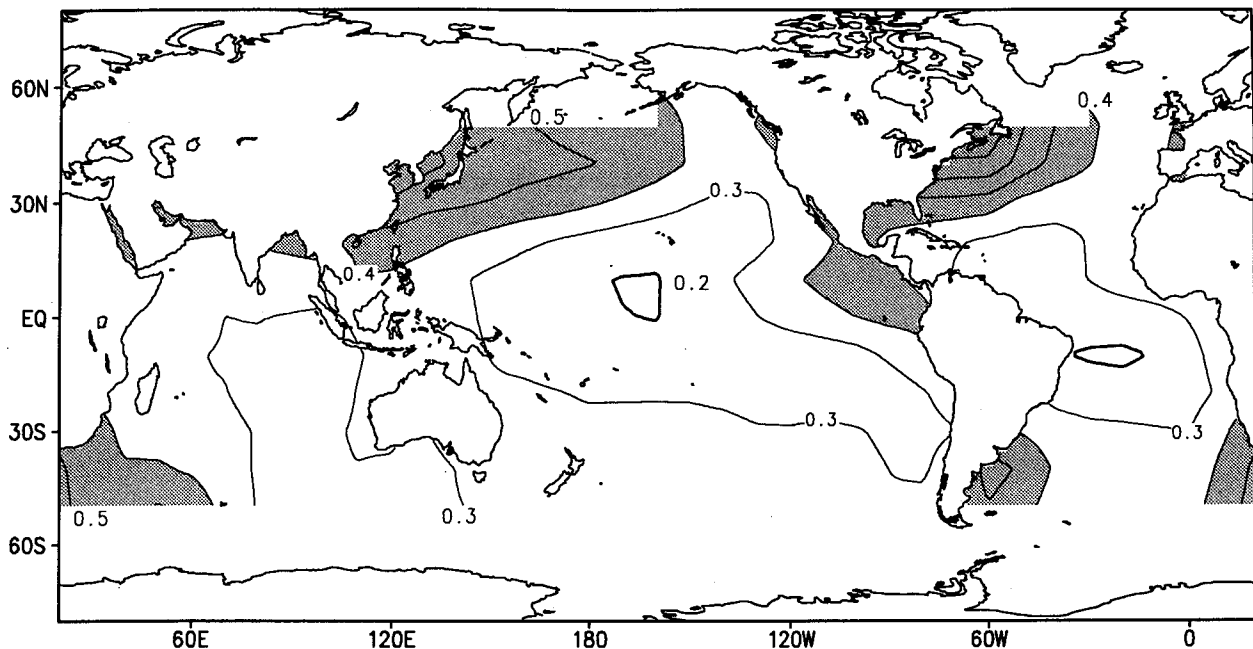
## Guess Error Standard Deviation (C)



FIG. 11. Guess error standard deviation ($\sigma_m$). The contour interval is 0.1°C. The 0.2°C contour
is a heavy line; values greater than 0.4°C are shaded.

A plot of the standard deviation of the guess error, $\sigma_m$, is shown in Fig. 11. The errors are lower in the Tropics and increase into the midlatitudes. They reach local maxima in the western boundary regions, especially in the Kuroshio and Gulf Stream regions. The guess errors are thus larger in regions where higher variability is expected. The magnitude of the guess error drops below 0.5°C over most of the ocean. It is difficult to distinguish guess differences less than 0.5°C using independent data. Thus, the size of the guess error seems to be too low. Some of the reduction is due to the detrending procedure, which reduces the variance by about 15%. This does not affect the ratios, $\epsilon$, because the detrending change affects both the numerator and the denominator.

The zonally averaged $\epsilon$ for each type of data is given in Fig. 12. Because the denominators of all the types of data are the same, this shows that the daytime and nighttime satellite and the buoy data increment errors are of roughly the same size while the errors for the ship data increments are much greater. Each type of data error tends to be roughly proportional to the guess error. Thus all are higher in midlatitudes than they are in the tropics. The figure shows that $\epsilon$ is roughly constant with latitude for the ratio of the ship data to guess error. However, the night satellite and the buoy $\epsilon$'s have a minimum in the tropics while the day satellite has a maximum. This day satellite maximum does not occur

at all tropical longitudes. The contribution is primarily from the western and central Pacific where the SSTs are subject to large diurnal cycles during periods with weak winds. It is important to recall that our "error" estimate includes space and time scales that the analysis cannot resolve. Thus, some of the daytime satellite error
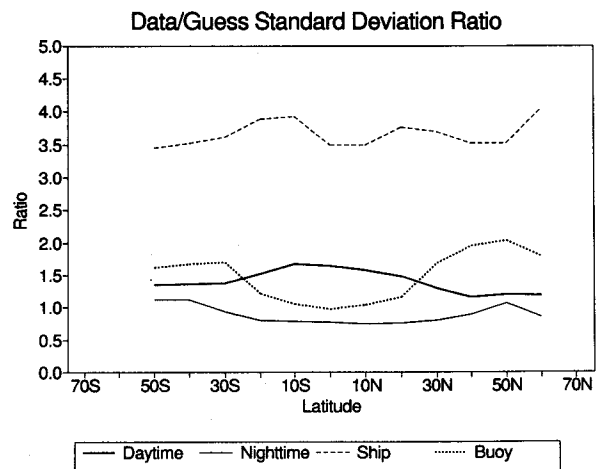
### Data/Guess Standard Deviation Ratio



FIG. 12. Zonally averaged data to guess standard deviation ratios: $\epsilon$. The values are shown for ships, buoys, daytime satellite, and nighttime satellite.

is due to the inability of the analysis to resolve the diurnal cycle. This may partially explain why the daytime satellite error is larger than the nighttime error.

Figure 13 shows the zonal average of the ratios, $\epsilon_c$ and $\epsilon_u$, which occur from splitting the satellite data increments into correlated and uncorrelated parts. In the tropics $\epsilon_c$ and $\epsilon_u$ are almost the same for the daytime satellite data. Outside the tropics the daytime value $\epsilon_c$ drops to half the size of $\epsilon_u$. Although the daytime $\epsilon_c$ is important, the nighttime $\epsilon_c$ is never very important, and it is defined as zero in the tropics by the definition of $\sigma_m^2$.

The global average of these "new" statistics is shown in Table 2 along with the "old" assumptions. The values for sea ice $\epsilon$ could not be easily calculated from the data. Thus, it was assumed that $\epsilon_c = 0$ and $\epsilon = \epsilon_u = 1$ for ice. This is roughly the same size as the value from the satellite and the buoys. The change in $\epsilon$ from old to new is relatively small and will have minimal impact on the OI.

The ship and buoy fields of $\epsilon$ were examined, but these fields seemed noisy and the differences could not be explained by ocean features. Thus, for ships and buoys, the global average value of $\epsilon$, given in Table 2, was used everywhere.

The $\epsilon$ determined in Table 2 greatly reduce the influence of ship observations on the OI compared with the other types of data. A simple example can help clarify this. Assume there are $n$ observations with uncorrelated errors at $n$ distinct locations. If the observations are close enough to the analysis point and each other that the exponent in (5) is equal to 1.0, then the weights, $w$, are equal and (2) reduces to
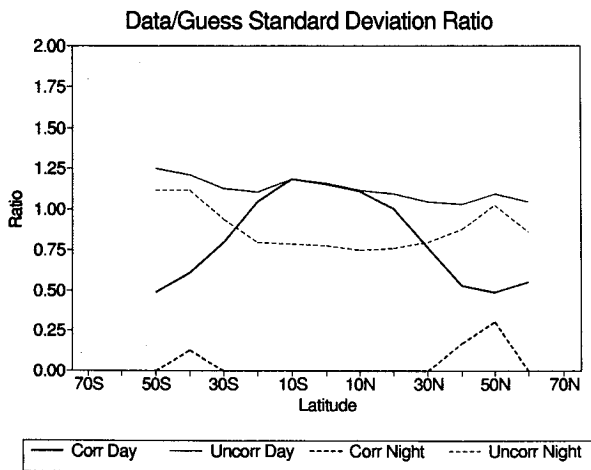
$$w = \frac{1}{\epsilon^2 + n}.$$

## Data/Guess Standard Deviation Ratio

FIG. 13. Zonally averaged correlated and uncorrelated data to guess ratios: $\epsilon_c$ and $\epsilon_u$, respectively. The values are shown for daytime satellite and nighttime satellite data.

TABLE 2. Global average ratio of data to guess error from the "new" statistics and the "old" assumptions.

Data/guess ratio: $\epsilon$

| Type of data | "New" statistics | "Old" assumptions |
|---|---|---|
| Ship | 3.9 | 3.0–1.8 |
| Buoy | 1.5 | 2.0–1.0 |
| Day satellite | 1.6 | 1.8–1.0 |
| Night satellite | 0.9 | 1.8–1.0 |
| Ice | 1.0 | 1.0 |

If the SST data increments are a constant, $q$, the analyzed SST, $r$, in (1) becomes

$$r = nwq = \frac{nq}{\epsilon^2 + n}. \tag{12}$$

Now we assume that we have one buoy observation and $n$ ship observations for which (12) is valid. If $q$ and $r$ are the same for the $n$ ship observations and the one buoy observation, then from (12) $n$ is defined by

$$n = \frac{\epsilon_s^2}{\epsilon_b^2},$$

where $\epsilon_b$ and $\epsilon_s$ are the buoy and ship values of $\epsilon$, respectively. Using the values in Table 2 for the new statistics, $n = 6.76$. In this example it takes almost seven ship observations to equal one buoy observation!

There is no reason to expect that the correlation $e$-folding scales should be the same for the guess and data errors. However, because the residuals were low and because of the noise in the $\lambda$'s, it was assumed that the scales were identical. The variables, $\lambda_x$ and $\lambda_y$, were computed from the fits using both daytime and nighttime satellite data increments. The two values of $\lambda_x$ and of $\lambda_y$ were qualitatively similar but spatially noisy. To improve the final product, the day and night $\lambda_x$ and $\lambda_y$ fields were first averaged. These averaged values of $\lambda_x$ and $\lambda_y$ were then smoothed by application of a five-point binomial smoother in both the meridional and zonal directions with weights: $1/16$, $4/16$, $6/16$, $4/16$, and $1/16$.

The smoothed $e$-folding scales (see Figs. 14 and 15) show that the zonal scales are larger than the meridional scales at most locations. Other studies (e.g., Clancy et al. 1990 and Meyers et al. 1991) have found the same result. However, along the west coast of North America, where upwelling produces a meridional band of cooler waters, the meridional scales are larger than the zonal scales. The meridional field is also noticeably flatter than the zonal field. Both fields show longer scales in midlatitudes than in the Tropics. There is also an indication of shorter scales in the eastern tropical Pacific, along 10°N, that suggests the influence of the intertropical convergence zone. However, there is only an indication of the shorter scales that could be expected
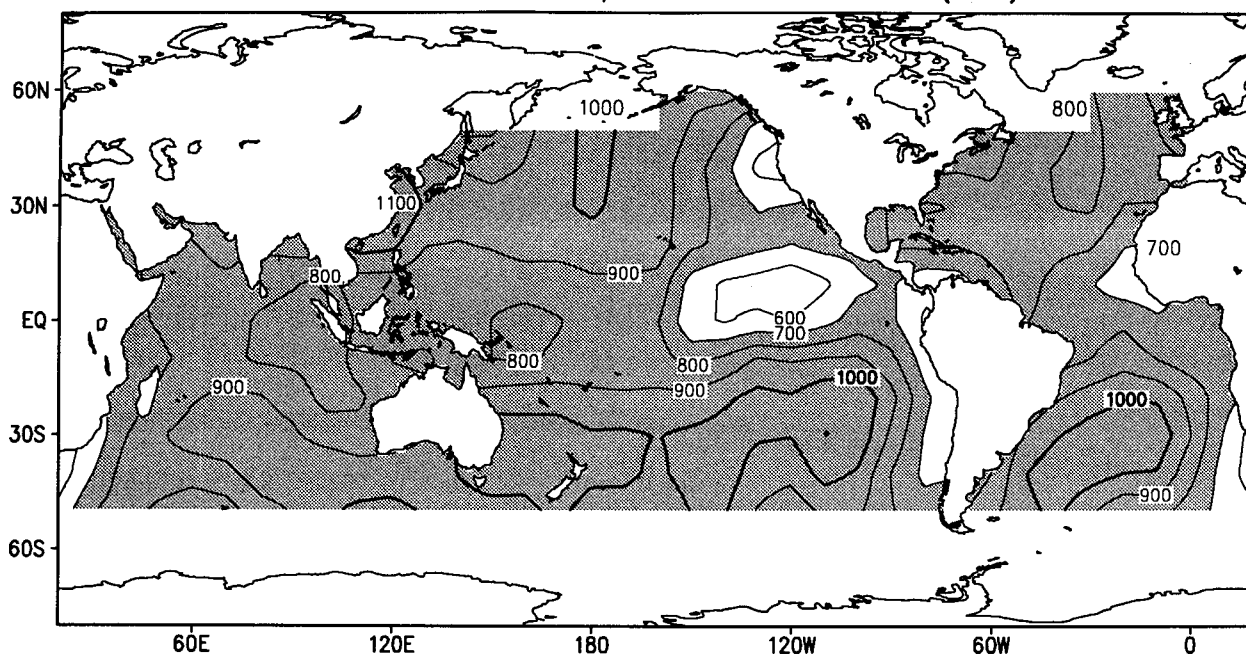
## Zonal Error Spatial Scales (km)



FIG. 14. The zonal error *e*-folding correlation scales, $\lambda_x$, derived from (6). The contour interval is 100 km.
The 1000-km contour is a heavy line; values greater than 700 km are shaded.

in the Kuroshio and Gulf Stream. The analysis on 20° boxes has degraded the resolution significantly. Thus, these scales should be considered only rough estimates. It will be necessary to extend the 1-yr period of study to improve the resolution.

The global average *e*-folding scales are shown in Table 3. These new scales are much greater than the assumed value. Although the scales are used for both the data and the guess, they do not imply that there are no data or guess signals on shorter scales.

Two versions of the OI were run. One used the "new" statistics and the other used the "old" assumptions. Both versions used their respective previous week's analysis as first guess. However, because there was no initial first guess for the analysis with the "new" statistics, the first pair of analyses began with the same first guess. The OI versions were run for a 4-week period to allow the differences to stabilize. The results of the OI with the new statistics are shown in Fig. 16. The OI with the old assumptions is shown in Fig. 5 for the same period. Comparison of the two figures shows that the OI with the new statistics is smoother than the OI with the old assumptions. This difference is primarily due to the change in the *e*-folding scales. The larger scales allow more data to influence the guess and thus result in a smoother field. As can be clearly seen in the figure, however, the new scales are not simply the min-

imum resolution of the guess. The minimum resolution is primarily determined by resolution of the SST signal in the data. This resolution of the OI is still finer than the 6° resolution of the blended field that is shown in Fig. 6. It is encouraging to see the small differences between Figs. 5 and 16. The large number of satellite and other SST data causes the OI to be relatively insensitive to the OI statistics.

To compare how well each analysis fits the data, we computed the rms of the data increments for both cases. The global value was 0.82°C using the old assumptions and 0.85°C using the new statistics. The rms differences were also computed for 20°-wide zonal bands. The analysis with the new statistics was always slightly larger. This increase of the rms should be expected because the analysis with the new statistics is smoother than the analysis with the old assumptions. The rms differences never exceeded 0.04°C, however. Thus, the improvement in the statistics only slightly degrades the overall fit of the data to the analysis.

It is difficult to compare these statistics with the statistics from other analyses. They depend on the spatial and temporal resolution of the analysis, the pre-OI data processing, and the first guess. The OI analysis of Clancy et al. (1990) and Clancy et al. (1992) includes an SST analysis that is similar to our analysis, although there are important differences. The more recent ver-

sion, Clancy et al. (1992), reports a "noise-to-signal ratio" that is equivalent to $\epsilon^2$. Their $\epsilon$ ranges from 1.2 to 2, which is roughly similar to the values in Table 2 and Fig. 12. Their values of the $e$-folding scales are roughly half of the values given here. These statistical differences are not surprising because of the analysis dissimilarities. However, the contrast between Figs. 5 and 16 suggests that the differences between our statistics and the statistics of Clancy et al. (1992) would not have a major impact on our SST results.

The OI theory (e.g., Lorenc 1981) also includes an estimate of the normalized error variance, $E$, defined at each grid point, $k$, by

$$E_k^2 = 1 - \sum_{i=1}^{N} w_{ik}\left\langle \pi_i \pi_j \right\rangle$$

following the notation in (1)–(3). The estimated normalized error will vary from one in regions where there is no data, to near zero in regions that are densely sampled by noise-free observations. The theoretical standard deviation for each analysis is then defined at each grid point as equal to $\sigma_m E$. Thus, the initial OI error, the first-guess error, is reduced by the factor $E$.

For the example shown in Fig. 16, the OI with the new statistics gives an average value of $E$ of 0.36. The

TABLE 3. Global $e$-folding scales from the "new" statistics and "old" assumptions.

Correlation scales (km): $\lambda$

| Direction | "New" statistics | "Old" assumptions |
|---|---|---|
| Zonal | 850 | 220 |
| Meridional | 615 | 220 |

average guess error (Fig. 11) is 0.36°C. This results in an average OI analysis error of only 0.13°C. The OI analysis error averaged only over the Tropics is even smaller, 0.08°C. The OI analysis errors for the example in Fig. 5 for the OI with the old assumptions are larger. The global average value is 0.29°C, while the average tropical value is 0.16°C. (These values were computed with the assumed constant guess error of 0.5°C that was used in the original statistics.)

The difference between the analysis errors shows that the analysis error is sensitive to the error statistics. This sensitivity is much greater than it is for the SST analysis increments. The error estimates for the analysis are probably too low. The normalized error, $E$, is strongly affected by the satellite data because of its dense coverage. The bias correction of the satellite data, which is discussed below, is done outside of the OI and is not
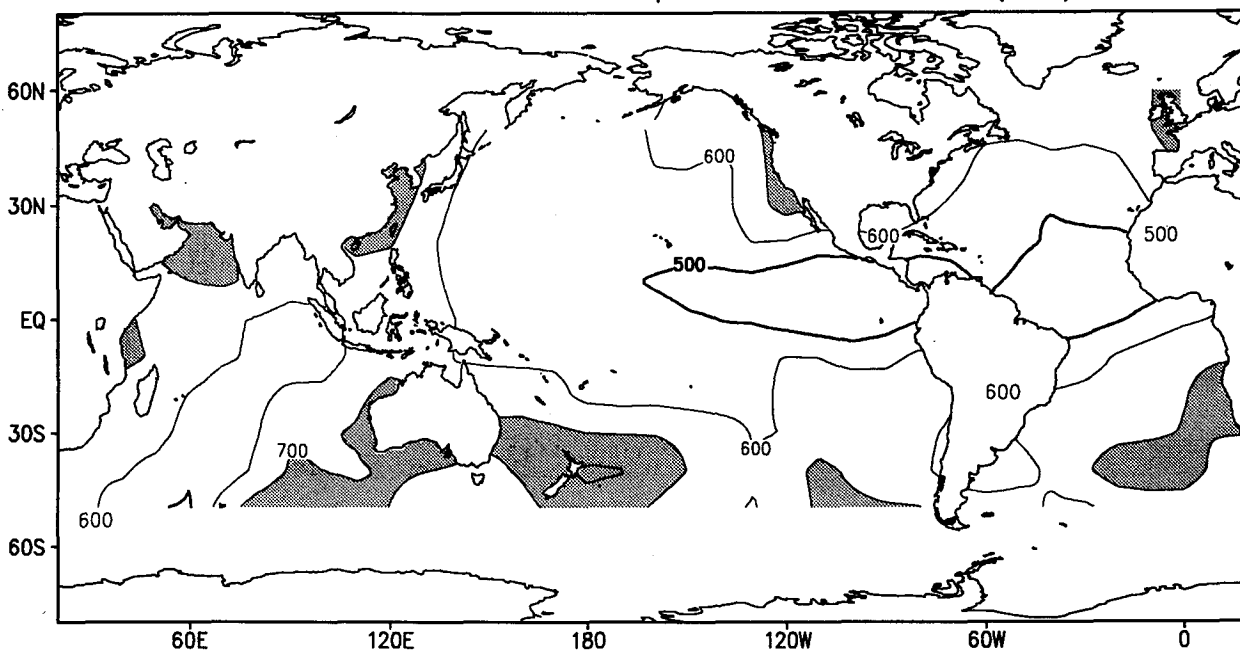


FIG. 15. The meridional $e$-folding error correlation scales, $\lambda_y$, derived from (7).
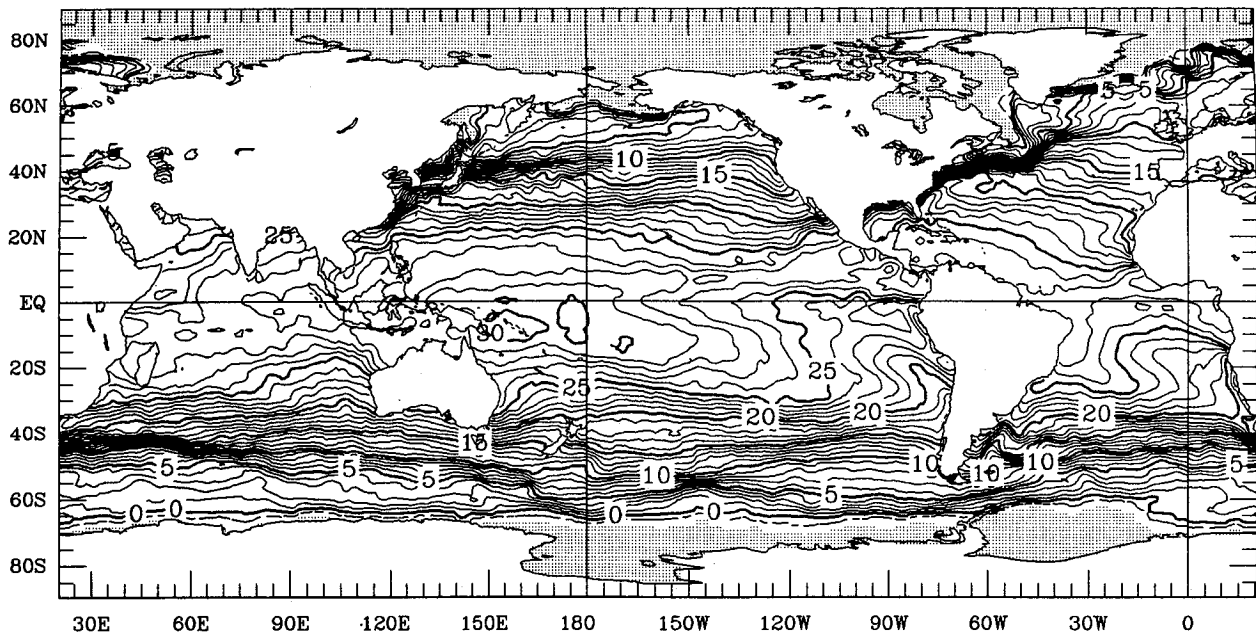The 500-km contour is a heavy line. Otherwise as in Fig. 14.

FIG. 16. Mean SST from the OI using the "new" statistics for the week 13–19 January 1991. Otherwise as in Fig. 5.

included in $E$, however. Thus, further effort is needed to define the analysis error estimate.

## 5. OI bias correction

The OI method assumes that the data are not biased. This is not always a valid assumption. Reynolds et al. (1989) compared several in situ and satellite analyses with independent expendable bathythermograph (XBT) data. These comparisons showed that most of the difference between the in situ and satellite data was due to satellite, not in situ, biases. They also demonstrated that the satellite biases could be different for daytime and nighttime retrievals. In addition, they showed that the largest biases during the 1982–89 period of record were due to stratospheric aerosols from the April 1982 volcanic eruptions of El Chichón. The usual retrieval algorithm adjusts for the attenuation by tropospheric water vapor, but it does not adjust for the different spectral attenuations by volcanic or other aerosols.

During June 1991, Mt. Pinatubo, located in the Philippines (15°N, 120°E), produced new stratospheric aerosols with a volume more than twice that from El Chichón (Stowe et al. 1992). As discussed in Reynolds (1993), the aerosols caused a severe reduction in the number of daytime satellite retrievals in the vicinity of the volcanic cloud but did not affect the number of nighttime retrievals. The sparsity of daytime observations can be seen relative to the nighttime observations by comparing Figs. 3 and 4. The change

occurred because different cloud detection procedures are used during the day than at night [see McClain et al. (1985) for details]. In addition, Reynolds (1993) shows that both daytime and nighttime retrievals had large-scale negative biases over the tropical oceans with magnitudes greater than 1°C. The biases in the nighttime retrievals are of greater importance for the OI because the number of nighttime observations remained high.

To correct for possible large-scale satellite biases, a preliminary step was added before performing the OI. This adjustment uses the Poisson technique of Reynolds (1988) and Reynolds and Marsico (1993) to provide a smooth correction field. In this method, preliminary in situ and satellite analyses are produced using spatial median filters to eliminate extremes. The in situ analysis uses ship and buoy SSTs as well as SSTs determined from sea ice information. Regions with sufficient in situ observations (presently five per grid box) become internal boundary conditions and regions that are ice covered become external boundary conditions. The SSTs for the remaining grid points are determined by solving Poisson's equation

$$\nabla^2 \Phi = \rho$$

for the SSTs, $\Phi$. The forcing term, $\rho$, is given by

$$\rho = \nabla^2 S,$$

where $S$ is the SST field defined by the satellite analysis. This method, the blended analysis, adjusts any large-

scale satellite biases and gradients relative to the boundary conditions defined by the in situ analysis.

The blended technique is used before the OI analysis to separately correct the daytime and nighttime retrievals. In this method three preliminary analyses are computed weekly on a 4° grid: an in situ, a daytime satellite, and a nighttime satellite. The median smoothing used in these analyses results in a spatial resolution of about 12°. Two blended analyses are produced: $\Phi_D$, produced by forcing with the Laplacian of the daytime satellite data, $\nabla^2 S_D$; and $\Phi_N$, produced by forcing with the Laplacian of the nighttime satellite data, $\nabla^2 S_N$. The smoothed daytime and nighttime correction fields are defined by $\Phi_D - S_D$ and $\Phi_N - S_N$, respectively. Both $\Phi_D - S_D$ and $\Phi_N - S_N$ are then spatially interpolated to the location of the daytime and nighttime data, as appropriate, and added to the data to provide the correction. Two versions of the weekly OI are computed: a version with in situ and corrected satellite data, and a version with in situ and uncorrected satellite data.

During 1991–92, two important biases occurred in the satellite data. The first bias was caused by the Mt. Pinatubo aerosols that affected the tropical satellite biases from July 1991 through April 1992. The second bias occurred south of 20°S between October 1991 and March 1992. This bias was primarily due to a nighttime satellite calibration error. This error (C. Walton 1992, personal communication) depends on the geometry of the satellite and the solar declination. It only occurs at middle and high southern latitudes during local summer. The error was made worse by the operational nighttime satellite algorithm adjustments that were used to correct the retrievals for the effect of the Mt. Pinatubo aerosols. In addition there were biases in both the daytime and nighttime retrievals caused by the additional stratospheric aerosols from the August 1991 eruptions of Mt. Hudson in Chile at 45°S. Reynolds (1993) discusses these biases in more detail.

To examine the effect of the aerosols on the retrieved SSTs, all weekly in situ, daytime, and nighttime satellite observations were separately averaged onto a 1° grid. These gridded values and the weekly OI analysis with and without the satellite bias corrections were converted into anomalies by subtracting the climatology given in Reynolds (1988).

The impact of the Mt. Pinatubo aerosols can be seen in the zonally averaged anomalies between 10°S and 10°N, which are shown in Fig. 17. The three data curves and the two analyses were within 0.5°C of each other from May through the end of June 1991. After this period, the in situ anomaly remained relatively constant while the day and night satellite anomalies became more negative. The nighttime anomalies reached a minimum during September. The daytime retrievals reached a minimum during August. The number of daytime observations was much sparser than

normal from August through October 1991, however. Thus, some change in the daytime satellite anomalies is due to undersampling of regions with high aerosol concentrations. The difference between the in situ and satellite anomalies shows that the satellite retrievals had average negative biases with magnitudes greater than 1°C in the tropics in August and September 1991. The change in the nighttime retrievals at the beginning of October was due to an adjustment of the retrieval algorithm to minimize the effects of the aerosols. The correction method is described in Walton (1985).

Figure 17 also shows that the OI without the bias correction (labeled OI) closely follows the nighttime retrieval anomaly except for a small offset during August and September. The offset is due to the small influence of the in situ data that eliminates roughly 0.2°C of the negative nighttime bias. The daytime retrievals had little influence because the number of observations was much lower than normal (see Figs. 3 and 4). The OI with the bias correction (labeled OI/Corrected) is within 0.2°C of the in situ curve everywhere with an average difference of less than 0.1°C.

The time series for the second area, which lies between 50°S and 30°S, is shown in Fig. 18. There the in situ anomalies remain relatively constant while the daytime and nighttime retrieval anomalies become more negative from August through October. The daytime retrievals reached a minimum in October and tended to move closer to the in situ curve with time. The daytime retrievals were not affected by the satellite calibration. Thus, any bias in the retrievals can be assumed to be from the Mt. Hudson aerosols. The nighttime retrieval anomalies reached a minimum in December. The difference between the nighttime satellite and in situ anomalies gradually diminished from December through April.

Figure 18 also shows that the OI anomalies without the bias correction closely follow the nighttime retrieval anomalies. This was because the number of daytime retrievals was roughly half the number of nighttime retrievals. In this example, the OI with the bias correction removed only half the difference between the in situ and nighttime anomalies. The bias correction here is not as effective as it was in the tropics because the in situ observations are more sparse (see Figs. 1 and 2). The sparsity of in situ observations is also suggested in the greater noise in the in situ curve compared to the in situ curve in Fig. 17.

## 6. Operational OI analysis

The daily version of the OI has been tested since August 1990. This version also uses 7 days of data with the same quality control and analysis technique as is used in the weekly version. The first guess is the analysis from the preceding day. Because the data from any one day would enter the analysis seven times during
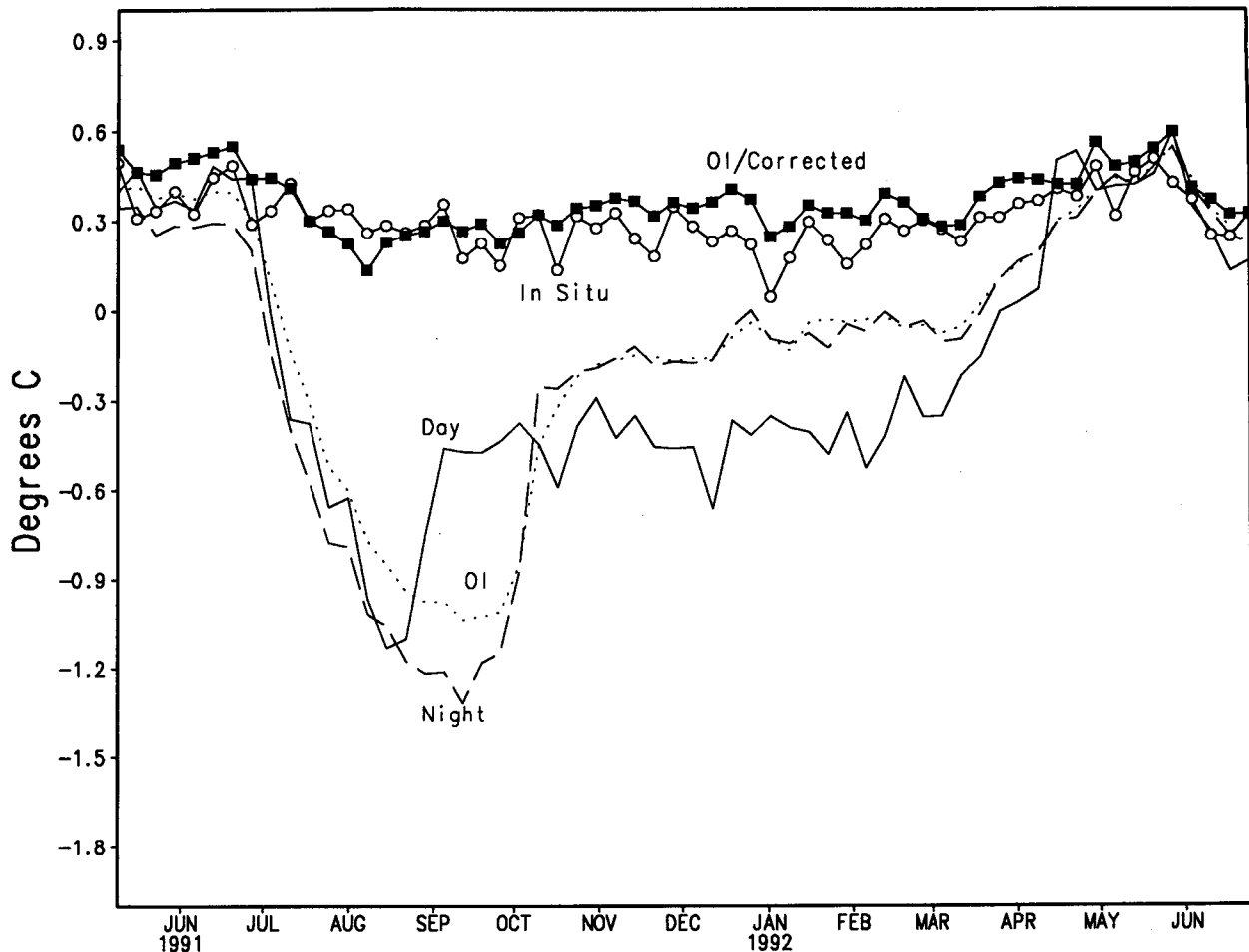
## SST Anomalies: 10S-10N



FIG. 17. Zonally averaged SST anomalies for the band from 10°S to 10°N. The curves show the in situ, the daytime and nighttime satellite data anomalies, and the OI anomalies with and without the satellite bias correction. The OI with the satellite bias correction is labeled "OI/Corrected."

one week, the data to guess error ratios, $\epsilon$, were increased by the square root of 7. This effectively gives the data the same weight in the daily and weekly versions because $\epsilon$ is squared in (3), which is the equation that defines the OI weights. Time series of the two versions indicate that the analyses are almost identical on weekly time scales. This agreement does not imply that there is no variability on daily scales. These scales have been filtered out by the use of 7 days of data.

The OI was operationally implemented at NMC on 20 February 1991. Because of operational restrictions, there has been only one version of the operational analysis. The daily OI was initially done without the satellite bias correction discussed in the preceding section. However, the volcanic aerosols had such a strong impact on the satellite data and, in turn, on the analysis

that the bias correction was urgently needed. This correction was added to the analysis on 29 July 1991. The statistics discussed in section 4 were implemented into the operational OI on 27 May 1992. The results were equivalent to the change in the weekly OI (compare Figs. 5 and 16) and resulted in a slightly smoother daily product.

When the OI was operationally implemented, the analysis provided the SST boundary condition for the NMC Medium Range Forecast (MRF) model. The operational MRF model was tested for an 11-day period using both the OI and a daily version of the blended analysis. The MRF showed some small improvement in the 5-day forecast temperatures (i.e., a few tenths of a °C) in the tropical troposphere when the SSTs were determined by the OI. Elsewhere the
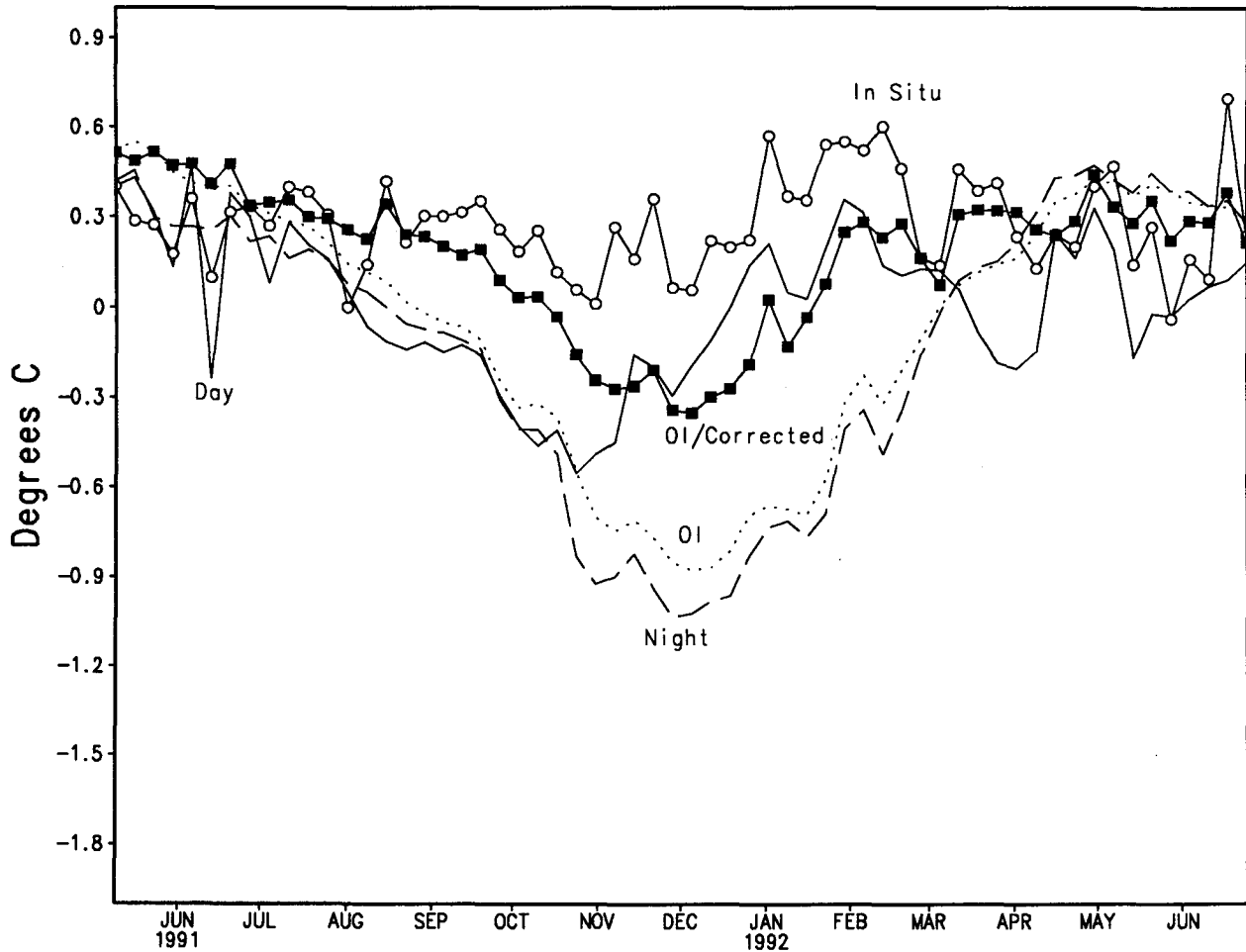
## SST Anomalies: 50S-30S



FIG. 18. Zonally averaged SST anomalies for the band from 50°S to 30°S. Otherwise as in Fig. 17.

difference between the two SST fields showed no significant change in the forecast temperature, humidity, or wind fields.

The current daily OI analysis is available on the GTS on a 2° grid. This 2° version is presently used as the SST boundary condition for forecast models at the European Centre for Medium-Range Weather Forecasts. The Japanese and Australian weather services have also expressed interest in the product. However, the daily product has not been available at either location because of hardware problems at the GTS node in Tokyo.

## 7. Discussion

The OI with the satellite bias correction is superior to the blended analysis because of its higher spatial and temporal resolution. The difference between the anal-

yses also is evident over large regions. The Niño 3 region in the eastern tropical Pacific (5°S–5°N; 150°W–90°W) has been used by modelers (e.g., Zebiak and Cane 1987) to verify ENSO forecasts. However, there are systematic differences between the two analyses in this region as shown in Fig. 19. Here, the monthly blended fields have been interpolated to the weekly resolution of the OI. The OI and blended curves are usually within 0.2°C of each other. Differences can reach 0.4°C, however. The figure shows that the OI tends to have more negative local minima and more positive local maxima than the blend. These differences tend to be larger during the local minima because the OI's higher resolution can better resolve equatorial upwelling.

To quantify the differences between the two curves in Fig. 19, we plan to use independent data. Preliminary

## SST Anomalies: 5N-5S; 150W-90W

FIG. 19. Average SST anomalies from the blend and the OI with the satellite bias correction
for the Niño 3 area: 5°S–5°N, 150°W–90°W.

results already show that the OI with the bias correction is superior to the blend in regions of high gradients (e.g., the eastern equatorial Pacific). These two analyses are almost identical in regions with almost no gradients (e.g., the western equatorial Pacific), however.

As mentioned at the end of section 4, the OI estimate of the tropical analysis error (using the new statistics) was less than 0.1°C. This analysis error is not exact because the satellite bias correction is not included in the normalized error estimate. However, the analysis error estimate would be statistically correct when the OI is used with uncorrected satellite data. In this case, the actual rms errors would also be much larger than 0.1°C because of the large biases in the satellite data (see Fig. 17). Although it will be difficult to determine if the OI is as good as the value suggested by the statistics, the use of independent data can help establish upper limits to these errors.

The error statistics determined in section 4 (see Table 2) tend to minimize the influence of the in situ data relative to the satellite. The major impact of the in situ data occurs in the bias correction of the satellite data before they are used in the OI. The spatial scales of the satellite and analysis errors shown in Figs. 14 and 15 indicate the scales of the correlated satellite error. Because our period of record in determining these statistics was only 1 year, the actual correlated scales are only approximated. Our results suggest that the satellite error scales are roughly 850 km in the zonal direction and 615 km in the meridional direction (see Table 3), however. It would be useful to be able to correct the satellite bias errors on these scales rather than the 12° scales used in the bias adjustments. We are actively working to develop new methods to use spatially varying correction scales.

In an earlier draft of this paper, J. Thiébaux (1992, personal communication) was concerned that the data increments used in the statistics were seasonally detrended while the data increments used in the OI were not. The change in the climatology during 1 week can exceed 1°C in middle and high latitudes. Thus, this difference could be important.

To examine this effect, the OI guess was corrected for the weekly change in climatology. Assume there has been an SST analysis, $S_{t-1}$, at time, $t-1$, and an analysis, $S_t$, is needed at time $t$. The uncorrected guess, $G^u$, used for the analysis of $S_t$ would be given by

$$G_t^u = S_{t-1}.$$

Between times $t$ and $t-1$, the SST climatology, $C$, would change by $(C_t - C_{t-1})$. Thus the climatologically corrected guess, $G^c$, would be given by

$$G_t^c = S_{t-1} + (C_t - C_{t-1}).$$

The OI was run with both the corrected and uncorrected guesses. The differences were very small (less than 0.25°C) over 95% of the ocean. However, the climatologically corrected guess could be very important if no new data were available for a long period. If there were no data, the use of the uncorrected guess is equivalent to assuming the mean SST persists; the use of the climatologically corrected guess is equivalent to assuming the anomaly SST persists. The persistence of the anomaly is physically more reasonable. Thus, the use of the climatologically corrected guess was added to the weekly analysis in August 1992 and was added to the operational analysis in October 1992.

As discussed throughout this manuscript, the OI has been evolving since it was first started in March 1990. To improve and extend these fields, the weekly OI has been computed or recomputed for the period January 1985 through December 1992 to present using the statistics derived in section 4 with the climatology correction. By the middle of 1994, the dataset will be extended back to November 1981. This is the practical limit because the AVHRR instrument first became operational in November 1981. Although the analyses will undoubtedly have to be processed several times to finalize the analysis procedure, a final product will be generated that uses consistent procedures throughout the entire period.

The OI analysis with the bias correction is still evolving. Once the OI has been analyzed from December 1981 to present, it is planned to recompute the statistics using the entire dataset. This will allow the refinement of the spatial resolution of the analysis and may allow the determination of the seasonal dependence. We believe that the OI with the bias correction is a significant improvement over the blended analysis and over any other analysis that uses uncorrected satellite data.

## APPENDIX

### Fitting Procedure

For each area, we require a least-squares fit of (6) or (7) to our binned correlations. If there are $n$ correlations, $F_i$, computed at separation distances, $d_i$, between the data values, then a function $E^2$ can be defined by

$$E^2 = \sum_{i=1}^{n} (F_i - \hat{F}_i)^2. \qquad \text{(A1)}$$

Here $\hat{F}_i$ are the model correlations given by (6) or (7) and written here in terms of $d_i$ as

$$\hat{F}_i = A \exp(-d_i^2/\lambda^2). \qquad \text{(A2)}$$

The parameters $A$ and $\lambda$ are determined by substituting (A2) into (A1) and requiring that

$$\frac{\partial E^2}{\partial A} = \frac{\partial E^2}{\partial \lambda} = 0.$$

This reduces to two equations

$$\sum_{i=1}^{n} F_i d_i^2 \exp(-d_i^2/\lambda^2)$$

$$- A \sum_{i=1}^{n} d_i^2 \exp(-2d_i^2/\lambda^2) = 0 \quad \text{(A3)}$$

and

$$\sum_{i=1}^{n} F_i \exp(-d_i^2/\lambda^2) - A \sum_{i=1}^{n} \exp(-2d_i^2/\lambda^2) = 0.$$

$$\text{(A4)}$$

From (A4), $A$ can be obtained in terms of $\lambda$ by

$$A = \frac{\sum_{i=1}^{n} F_i \exp(-d_i^2/\lambda^2)}{\sum_{i=1}^{n} \exp(-2d_i^2/\lambda^2)}. \qquad \text{(A5)}$$

Substituting (A5) into (A3) gives

$$\sum_{i=1}^{n} F_i d_i^2 \exp(-d_i^2/\lambda^2) \sum_{i=1}^{n} \exp(-2d_i^2/\lambda^2) - \sum_{i=1}^{n} d_i^2 \exp(-2d_i^2/\lambda^2) \sum_{i=1}^{n} F_i \exp(-d_i^2/\lambda^2) = 0. \quad \text{(A6)}$$

The value of $\lambda$ is found by numerically solving (A6) by trial and error using different $\lambda$'s at 5-km intervals. Once $\lambda$ is found, $A$ is given by (A5).

## REFERENCES

Buell, C. E., and R. S. Seaman, 1983: The 'scissors' effect: Anisotropic and ageostrophic influences on wind correlation coefficients. *Aust. Meteor. Mag.,* **31,** 77–83.

Clancy, R. M., P. A. Phoebus, and K. D. Pollak, 1990: An operational global-scale ocean thermal analysis system. *J. Atmos. Oceanic Technol.,* **7,** 233–254.

——, J. M. Harding, K. D. Pollak, and P. May, 1992: Quantification of improvements in an operational global-scale ocean thermal analysis system. *J. Atmos. Oceanic Technol.,* **9,** 55–66.

Gandin, L. S., 1963: *Objective Analysis of Meteorological Fields.* In Russian, Gidrometeor. Isdat., Leningrad. [English translation, 1966, Israeli Program for Scientific Translations. Jerusalem, 242 pp.]

Lorenc, A. C., 1981: A global three-dimensional multivariate statistical interpolation scheme. *Mon. Wea. Rev.,* **109,** 701–721.

McClain, E. P., W. G. Pichel, and C. C. Walton, 1985: Comparative performance of AVHRR-based multichannel sea surface temperatures. *J. Geophys. Res.,* **90,** 11 587–11 601.

Meyers, G. H. Phillips, N. Smith, and J. Sprintall, 1991: Space and time scales for optimal interpolation of temperature-tropical Pacific Ocean. *Progress in Oceanography,* Vol 28, Pergamon 189–1991.

Rasmusson, E. M., and T. H. Carpenter, 1982: Variations in tropical sea surface temperature and surface wind fields associated with the Southern Oscillation/El Niño. *Mon. Wea. Rev.,* **110,** 354–384.

Reynolds, R. W., 1978: Sea surface temperature anomalies in the North Pacific. *Tellus,* **30,** 97–103.

——, 1988: A real-time global sea surface temperature analysis. *J. Climate,* **1,** 75–86.

——, 1993: Impact of Mount Pinatubo aerosols on satellite-derived sea surface temperatures. *J. Climate,* **6,** 768–774.

——, and D. C. Marsico, 1993: An improved real-time global sea surface temperature analysis. *J. Climate,* **6,** 114–119.

——, C. K. Folland, and D. E. Parker, 1989: Biases in satellite derived sea-surface-temperatures. *Nature,* **341,** 728–731.

Stewart, G. W., 1973: *Introduction to Matrix Computations.* Academic Press, 441 pp.

Stowe, L. L., R. M. Carey, and P. P. Pellegrino, 1992: Monitoring the Mt. Pinatubo aerosol layer with *NOAA/11* AVHRR data. *Geophys. Res. Lett.,* **19,** 159–162.

Thiébaux, H. J., and M. A. Pedder, 1987: *Spatial Objective Analysis: With Applications in Atmospheric Science.* Academic Press, 299 pp.

——, L. L. Morone, and R. L. Wobus, 1990: Global forecast error correlations. Part 1: Isobaric wind and geopotential. *Mon. Wea. Rev.,* **118,** 2117–2137.

Walton, C. C., 1985: Satellite measurement of sea surface temperature in the presence of volcanic aerosols. *J. Climate Appl. Meteor.,* **24,** 501–507.

——, 1988: Nonlinear multichannel algorithms for estimating sea surface temperature with AVHRR satellite data. *J. Appl. Meteor.,* **27,** 115–124.

Zebiak, S. E., and M. A. Cane, 1987: A model of El Niño–Southern Oscillation. *Mon. Wea. Rev.,* **115,** 2262–2278.